Experimental and Theoretical Investigation of A Coaxial Inverse-Pinch Pulsed Plasma Thruster II [1]

Hani Kamhawi
The Ohio State University
Columbus, OH 43220
Hani.Kamhawi@grc.nasa.gov

Pavlos G. Mikellides
Ohio Aerospace Institute
Brook Park, OH 44142
PavlosMikellides@oai.org

Peter J. Turchi
Los Alamos National Laboratory
turchi@lanl.gov

IEPC-01-162

A coaxial inverse-pinch pulsed plasma thruster (PPT) has been designed, fabricated, and tested. Experiments were performed to measure the thruster's discharge current, Teflon mass loss rate, spatial and temporal magnitudes of the azimuthal magnetic field strength in the thruster's inter-electrode region, and temporal profiles of the electron temperature (T_e) and number density (n_e) in the thruster's plume using triple - Langmuir probes. Results from the azimuthal magnetic field probes confirmed the attainment of an azimuthally symmetric current distribution. T_e values between 3 and 8 eV and n_e values up to 10^{21} m^{-3} were measured in the thruster's plume. The MACH2 2-½ magnetohydrodynamic code was utilized to model the thruster operation. The MACH2 predicted current waveforms, enclosed current magnitudes, and T_e and n_e temporal profiles agreed well with experimental data.

INTRODUCTION

Pulsed plasma thrusters (PPTs) are simple, robust, and easy to operate devices but are governed by complex physical processes. Parallel-rail and coaxial geometry pulsed plasma thrusters (PPTs) have been designed, investigated, and evaluated over the past 30 years. Parallel-rail thrusters have flown on satellites and are currently flying on the Earth Observer 1 (EO-1) mission [1]. However, PPTs low efficiency (<15%) have limited their use and application in more missions. To improve thruster performance, numerical studies were directed at theoretically investigating and evaluating solid Teflon pulsed coaxial thrusters. Annular, linear, and coaxial configurations were evaluated [2]. Results indicated that a coaxial inverse-pinch configuration with a symmetric current distribution on the propellant surface allowed the attainment of high peak currents while limiting Teflon surface temperatures below the Teflon decomposition

[1]. Presented as Paper IEPC-01-162 at the 27th International Electric Propulsion Conference, Pasadena, CA, 15-19 October, 2001

temperature of approximately 673 K. Limiting Teflon Temperature below 673 K limits post-pulse evaporation and macroparticle evolution [2].

Based on these earlier theoretical studies, a coaxial inverse-pinch PPT was designed, fabricated, and tested. The first configuration tested employed two RG-58 coaxial cables along with a Unison ignition exciter circuit to initialize the PPT capacitor energy discharge. The two ignition leads were placed 0.51 cm from the face of the Teflon surface and are 180^{o} apart. Azimuthal magnetic field mappings were performed at different radial and axial locations to validate current symmetry. Results showed that for the two cable ignition configuration, the current distribution at a radial location of 1.5 cm was not symmetric, this results in non-uniform heating of the propellant surface and subsequently non-uniform ablation which results in inefficient thruster operation. As a result, a new configuration was designed, fabricated, and tested. In this new configuration, the ignition cable was placed inside the center electrode, cathode. Initial results of testing were presented in Ref. 3. A detailed description of this configuration will be presented in this paper.

This paper presents recent experimental efforts aimed at operating a coaxial inverse-pinch PPT with a symmetric current distribution in the thruster's inter-electrode region which would allow for comparisons with numerical simulations from the MACH2 code. To accomplish this, the azimuthal magnetic field was mapped at different azimuthal, radial, and axial locations to confirm current symmetry. In addition, Teflon mass loss and triple-Langmuir probe measurements were performed.

EXPERIMENTAL FACILITIES AND COAXIAL INVERSE-PINCH PULSED PLASMA THRUSTER DESIGN:

Experimental investigation of the coaxial inverse-pinch PPT was performed at NASA Glenn Research Center (GRC) Electric Propulsion Research Laboratory. Experiments were performed in VF-3. VF-3 has diameter of 1.5 m and is 4.5 m long. The facility was used because it could be evacuated to a pressure as low as $3X10^{-3}$ Torr with the backing roughing pumps or it can be evacuated to a pressure as low as $2X10^{-6}$ Torr using oil-diffusion pumps that are backed by the roughing pumps. In addition, the torsional type thrust stand used to measure thrust and impulse bit for PPTs can be installed in VF-3 [4].

A picture of the coaxial inverse-pinch PPT is presented in Figure 1 and a detailed schematic of the thruster is presented in Figure 2. A Maxwell oil-filled 33.2 µF capacitor is utilized. The capacitor has a cylindrical metal case whose diameter is 8.4 cm and is 8.9 cm long. In addition, the hot stud is located at the center of the cylinder and is surrounded by a ground ring. The ground ring has an inner diameter of 5.1 cm and an outer diameter of 6.35 cm. The capacitor is rated for a maximum voltage and current of 2000 volt and 25 kA, respectively. Figure 1 and 2 show the aluminum nozzle-shaped anode electrode. The center, initially cathode, electrode houses the ignition cable which initiates the PPT breakdown. The aluminum transmission lines are U-shaped, this construction was necessary since the capacitor's center stud was positive, whereas, the thruster's outer electrode, nozzle, is the anode. Figure 3 shows detailed dimensions of the coaxial inverse-pinch PPT inter-electrode region. From Figure 3, it is shown that the Teflon propellant has a radius 1 cm, the center electrode has a radius of 1.35 cm, the outer nozzle-electrode has a radius of 3.87 cm, and the gap between the electrodes is 1.6 cm.

EXPERIMENTAL RESULTS

Testing of the coaxial inverse-pinch PPT at the Ohio State University Aeronautical and Astronautical Research Laboratory (AARL) vacuum facility at a background pressure of $3X10^{-3}$ Torr indicated a symmetric current distribution. Figure 4 presents the discharge image at peak thruster current, the image indicated a discharge that is symmetric. As a result, recent testing in VF-3 was performed at a

background pressure of $3X10^{-3}$ Torr, since earlier testing at a background pressure of $5X10^{-5}$ Torr failed to achieve an azimuthally symmetric current discharge [3].

For this study, experimental results obtained include the current waveforms, azimuthal magnetic field mappings in the inter-electrode region, and Teflon mass loss measurements for 20 and 30 joule thruster operation. Electron temperature (T_e) and number density (n_e) mappings in the plume of the PPT were performed for 20 joule thruster operation. Theoretical and numerical simulations with the MACH2 code will be presented and compared to the experimental results.

CURRENT WAVEFORMS

The coaxial-inverse pinch PPT discharge current was measured with a 31 turn Rogowski coil potted around the capacitor positive stud. The output of the Rogowski coil was integrated with an RC integrator, it has a calibration number of $1.15\ X10^4$ amp/volt. Figure 5 presents the discharge current waveforms for energy levels of 20 and 30 joule. Peak currents of 18.6 and 24 kA are attained for energy levels of 20 and 30 joule, respectively.

TEFLON MASS LOSS MEASUREMENTS

Teflon Mass loss measurements were performed in VF-3. Tests were performed for the thruster configuration depicted in Figure 3. For 20 joule thruster operation at a repetition rate of 1.24 Hz, Teflon mass loss per pulse was 3.72 μg/pulse for 2530 pulses. For 30 joule thruster operation at a repetition rate of 1.22 Hz, Teflon mass loss was 11.54 μg/pulse for 745 pulses and 10.2 μg/pulse for 1167 pulses. Inspection of the Teflon propellant after each test indicated that the surface of the Teflon was lightly and uniformly carbonized. It is important to note that after each test, the thruster was disassembled and a new ignition cable was installed. This was done after it was observed that after about 2500 pulses the ignition cable tip carbonizes and the PPT discharge initiation becomes sporadic and random.

MAGNETIC FIELD MAPPINGS

Azimuthal magnetic field mappings were performed in the inter-electrode region of the coaxial inverse-pinch PPT discharge shown in Figure 3. Three probes have been constructed and are made of 4 turns of 30 gauge magnetic wire, they have an inner diameter of 1 mm. The probes and the twisted pair of magnetic wire are enclosed in a pyrex tube which has an inner diameter of 1.4 mm and an outer diameter of 3 mm; the tube is 25 cm long and is closed at one end. At the tube open end the pair of magnetic twisted wire are connected to a RG-174U miniature coaxial cable. The output signals from all three probes are integrated with an RC integrator with a time constant of 10 μsec. The probes are calibrated using a setup utilizing the coaxial inverse-pinch PPT, they are calibrated each time they are setup for a given radial location. The probes have an accuracy of ±13% and the uncertainty is mainly attributed to uncertainty in the current measurement and radial probe positioning. Measurements were made at radial locations of 1.59, 2, and 3 cm for axial locations of 0, 0.5, 1, 1.5, 2, and 2.5 cm from the anode electrode face. At each location measurements were simultaneous made at three azimuthal location of 0^o, 90^o, and 180^o. Tests were performed for energy levels of 20 and 30 joule.

Previous magnetic field mappings on the coaxial inverse-pinch PPT [3,5]were performed in a small vacuum facility were a ground-plane was extended and connected from the Faraday cage to inside the vacuum facility. However, since pressure limitations required testing in VF-3, which has no proper grounding plane, EMI became an issue and that required filtering of the B-probe signals using a FFT routine. Figure 6 shows magnetic probe signals at a radial location of 1.59 cm and an axial location of 0 cm for an energy level of 20 joule. Figure 7 shows the magnetic probe signals after the high-frequency noise was filtered out with the FFT

routine and multiplied by the appropriate probe calibration numbers.

For 20 joule operation, Figures 8, 9, and 10 present azimuthal magnetic field mappings at radial locations of 1.59, 2, and 3 cm for the different axial locations. For all radial and axial locations and within the accuracy of the probes, the output of the three probes indicates an azimuthally symmetric current discharge. The enclosed current magnitude is calculated using

$$I_{encl} = \frac{2\pi r B_\theta}{\mu_o} \qquad (1)$$

where B_θ is the azimuthal magnetic field strength in Tesla, r is the radial location in meter, and μ_o is the permeability of free space and is equal to $4\pi X10^{-7}$henries/m. For a radial location of 1.59 cm and at axial locations of 0, 0.5, 1, 1.5, 2, and 2.5 cm from the surface of the anode electrode the enclosed current magnitudes are 19, 18.3, 17.5, 11.1, 8.7, and 4.8 kA, respectively. For a radial location of 2 cm and at axial locations of 0, 0.5, 1, 1.5, 2, and 2.5 cm from the surface of the anode electrode the enclosed current magnitudes are 19, 17, 16, 11, 15, 15, and 10 kA, respectively. For a radial location of 3 cm and at axial locations of 0, 0.5, 1, 1.5, 2, and 2.5 cm from the surface of the anode electrode the enclosed current magnitudes are 16.5, 13.5, 12, 10.5, 13.5, and 9 kA, respectively.

For 30 joule operation, Figures 11,12, and 13 present azimuthal magnetic field mappings at radial locations of 1.59, 2, and 3 cm for the different axial locations. Results indicate that within the probe accuracy, the current discharge is azimuthally symmetric. For a radial location of 1.59 cm and at axial locations of 0, 0.5, 1, 1.5, 2, and 2.5 cm from the surface of the anode electrode the enclosed current magnitudes are 20, 22, 20.7, 16.7, 12.7 , and 5.6 kA, respectively. For a radial location of 2 cm and at axial locations of 0, 0.5, 1, 1.5, 2, and 2.5 cm from the surface of the anode electrode the enclosed current magnitudes are 20, 20, 17, 16, 14, and 8 kA, respectively. For a radial location of 3 cm and at axial locations of 0, 0.5, 1, 1.5, 2, and 2.5 cm from the surface of the anode electrode the enclosed current magnitudes are19.5, 18, 13.5, 15, 12, 10.5 kA, respectively.

ELECTRON TEMPERATURE AND NUMBER DENSITY MEASUREMENTS

To further investigate the behavior of the inverse-pinch PPT thruster, electron temperature (T_e) and electron number density (n_e) measurements were performed in the PPT plume. Single, double, and triple--Langmuir probe can be used to obtain T_e and n_e magnitudes and spatial and temporal profiles in the PPT plume. For this experiment, a triple-Langmuir probe will be utilized, it permits the instantaneous measurement of the plasma temperature and number density without the need for voltage sweeps or subsequent construction of the probe current-voltage characteristics curve needed to obtain T_e and n_e from single and double-Langmuir probe raw data [6,7]. Since PPTs are characterized by high frequency oscillations, the use of a triple-Langmuir probe will greatly reduce the effort and time required for data reduction and will reduce the uncertainty in the T_e and n_e measurements due to shot to shot variations in the PPT operation.

Langmuir probes are simple probes but the theory governing their behavior and operation is complicated and is dependent on their domain of operation. Langmuir probes domain of operation can be determined by evaluating a number of parameters. These parameters are the probe radius(r_p), Debye Length(λ_D), Mean free path(λ), and probe separation(s). The Debye Length, λ_D, which is a measure of the shielding or sheath thickness is given by

$$\lambda_D = \sqrt{\frac{\varepsilon_o k T_e}{n_e e^2}} \qquad (2)$$

where ε_o is equal to $8.854X10^{-12}$ F/m and is the permittivity of free space, k is equal to $1.381X10^{-23}$ J/K and is the Boltzmann constant, and e is equal to $1.609X10^{-19}$ Coul and is the electron charge. The mean free path, λ, which is the distance a particle

travels before it experiences a collision is given by

$$\lambda_{i-i} \approx \lambda_{i-e} \approx \lambda_{e-e} \approx 3.4X10^{13} \frac{T_e^2(eV)}{n_e(cm^{-3})\ln(\Lambda)} \quad (3)$$

where $\ln(\Lambda)=10$.

From previous studies, for typical PPT operation, T_e ranges between 3 to 8 eV and n_e ranges between 10^{19} to 10^{21} m^{-3}. For T_e between 3 and 8 eV and for n_e below $10^{21}m^{-3}$, the Knudson number and λ_D/r_p are greater than 1, whereas for n_e values above $10^{21}m^{-3}$ the Knudson number is below 1. Thus according to Ref. [8] and based on the number densities predicted for the coaxial inverse-pinch PPT, the Triple Langmuir probe is operating in the domain of a conventional thin sheath for a probe radius of 0.127 mm.

The triple-Langmuir probe used in this study was constructed from three identical 0.254 mm diameter Tungsten wires that are inserted into a 4 hole 3.175 mm O.D. alumina rod that is 30 cm long, The exposed length of the Tungsten wires is 6 mm. Figure 14 presents a schematic of the probe circuitry, probes 2 and 3 are biased to negative voltages V_{d2} and V_{d3} with respect to probe 1 as shown in the probe potential diagram presented in Figure 14. V_{d2} was set to 4.81 volt which was applied via 3 size D batteries connected in series, whereas, V_{d3} was set to 18.74 volt which was applied via 2 9 volts batteries. Taking the current directions shown in Figure 14 as being positive and assuming that the electron energy distribution is Maxwellian, and since the probe is operating in a regime where the mean free path is greater than the probe radius (Knudson number >1), the mean free path is greater than the Debye length, and the Debye length is much less than the separation between the different probe wires, the following equations describe the currents that are collected by the probes and are given by [6]

$$-I_1 = -SJ_e \exp(-\phi V_1) + SJ_i(V_1) \quad (4)$$

$$I_2 = -SJ_e \exp(-\phi V_2) + SJ_i(V_2) \quad (5)$$

$$I_3 = -SJ_e \exp(-\phi V_3) + SJ_i(V_3) \quad (6)$$

where J_i is the ion saturation current ($J_i=en_e(kT_e/(2\pi m_e))^{1/2}$), S is the surface area of the probe, and J_e is the electron saturation current density caused by the thermal electron diffusion to the probe ($J_e=en_e(kT_e/(2\pi M_i))^{1/2}$), and $\phi=e/(kT_e)$. To determine T_e, equations 4, 5 , and 6 have to be solved simultaneously with the assumption that $J_i(V_1) \sim J_i(V_2) \sim J_i(V_3)$ which yields [6]

$$\frac{I_1+I_2}{I_1+I_3} = \frac{1-\exp(-\phi V_{d_2})}{1-\exp(-\phi V_{d_3})} \quad (7)$$

To determine the electron temperature equation 7 is used. Using the values of V_{d2} and V_{d3} applied for current collection, and by measuring the currents flowing in probes 2 and 3, T_e is found using equation 7. For the coaxial inverse-pinch PPT T_e measurements, Figure 15 provides a curve of the electron temperature for different current ratios for V_{d2} and V_{d3} values of 4.81 and 18.74 volts, respectively.

To calculate the electron number density (n_e), once T_e is determined, and assuming equal ion and electron number densities, n_e can be calculated by [6]

$$n_e = \frac{1}{S}\frac{I_3 - I_2\exp(-\phi\Delta V_d)}{1-\exp(-\phi\Delta V_d)}\frac{\exp(-0.5)}{e\sqrt{\frac{kT_e}{m_i}}} \quad (8)$$

where $\Delta V_d=V_{d3}-V_{d2}=V_3-V_1$. The value of T_e and n_e from equations 7 and 8 represent a first estimate of the electron temperature and number density. Next, corrections must be made to the ion current to account for differences in the ion current due to application of V_{d2} and V_{d3}. To accomplish this, the

Peterson /Talbot curve-fit [7,8] is used and is given by

$$J_i(\phi V) = J_{io}(B + \phi V)^{\alpha} \quad (9)$$

where

$$\alpha = \frac{2.9}{\ln(\frac{r_p}{\lambda_D})} + 0.07(\frac{T_i}{Z_i T_e})^{0.75} - 0.34 \quad (10)$$

$$B = 1.5 + (0.85 + 0.135\ln(\frac{r_p}{\lambda_D})^3)\frac{T_i}{Z_i T_e} \quad (11)$$

Applying equation 9 to equations 4, 5, and 6, equation 7 becomes

$$\frac{I_1 + I_2}{I_1 + I_3} = \frac{-J_e[(\exp(-\phi V_2) - \exp(-\phi V_1)] + J_{io}[(B+\phi V_2)^{\alpha} - (B+\phi V_1)^{\alpha}]}{-J_e[(\exp(-\phi V_3) - \exp(-\phi V_1)] + J_{io}[(B+\phi V_3)^{\alpha} - (B+\phi V_1)^{\alpha}]} \quad (12)$$

To calculate n_e equations 5 and 6 are used with the proper corrections to J_i, n_e can be expressed as

$$n_e = \frac{\sqrt{2\pi}}{e\sqrt{\frac{kT_e}{M_i}}}\frac{1}{S}\frac{I_3 - I_2\exp(\phi V_2 - \phi V_3)}{(B+\phi V_3)^{\alpha} - (B+\phi V_2)^{\alpha}\exp(\phi V_2 - \phi V_3)} \quad (13)$$

It is important to note that the floating potential (V_f) can be calculated using equations 4 or 5 or 6 by setting the left hand side of the equation equal to zero and solving for V_f that satisfies that equation. However, to calculate T_e and n_e in equations 12 and 13, respectively, it is necessary to find V_2 that satisfies equation 5 for the measured value of I_2, this is necessary to properly account for the corrections to the ion current. Once V_2 is found, V_1 and V_3 are found as shown in Figure 14.

To determine the values of T_e and n_e for measured I_2 and I_3 currents, equation 7 is used to determine T_e. Then n_e is found using equation 8. This first approximation of T_e and n_e is then used in the Peterson/Talbot correction equations [7,8]. The values of B, α, V_f, and V_2 are calculated as outlined in the earlier discussion. Then using equations 12 and 13 , corrected values of T_e and n_e are found. Once the corrected T_e and n_e values are found they are used again in the Peterson/Talbot correction equations (9-11), and the iterative procedure is repeated until the difference between successive T_e values is below a prescribed tolerance.

Measurements were performed in the plume of the coaxial inverse-pinch PPT. Measurements were performed at radial locations 2, and 3 cm from the thruster axis at an axial distances of 6 cm from the thruster's exit plane. Measurements were performed for an energy level of 20 joule. Tektronix A6303 current probes and AM503A current probe amplifiers were used to acquire I_2 and I_3. The measured current waveforms were recorded on a Lecroy 9314 digital oscilloscope. The measured current waveforms have an accuracy of 10%. Figure 16 presents typical I_2, and I_3 Langmuir probe current waveforms at a radial location of 3 cm at an axial distance of 6 cm from the thruster's exit plane. Probe cleaning, while testing, was not utilized in this study due to facility limitations. At each location, 10 measurements were performed and recorded. Inspection of the Tungsten wires after each run indicated that no observable contamination was occurring. An error in the measured I_2 and I_3 of 10% each can result in a error of up to 15% in the current ratio(i.e, ([I1+I2]/[I1+I3]). The effect of an error in the current ratio on T_e depends on the magnitude of the current ratio since the slope of the curve, shown in Figure 15, increases drastically for smaller current ratio magnitudes. In general, if the current ratio magnitude is above 0.6 the error in T_e is ±1 eV, whereas, for current ratio values between 0.5 and 0.6 the error in T_e is ± 1.5 eV. For current ratio magnitudes below 0.5, the error increases dramatically and the measurement accuracy drops. For number density accuracy, the accuracy of the measurement is 60% [7] and is mainly attributed to the error in the probe current measurements and the subsequent error it causes on the electron temperature. Additionally, error due to shot-to-shot variations has not been fully investigated since no probe cleaning setup was available at VF-3. Error due to presence of multiply ionized species and

transverse electron drift has not been investigated here but is estimated to be around 10% [7].

Figures 17, 18, 19, and 20 present T_e and n_e temporal variations at radial locations of 2 and 3 cm for an axial distance of 6 cm from the thruster's exit plane for 20 joule thruster operation, respectively. Results presented in Figures 17, 18, 19, and 20 will be discussed in the next section.

THEORETICAL MODELING

The time dependent 2 ½-dimensional magnetohydrodynamic MACH2 code [9], developed by the Mission Research Corporation and modified at the Ohio State University, is a single fluid, multi-temperature, time-split model, real equation of state (EOS), real viscosity effects, and anomalous transport solver. The code utilizes multi-grid diffusion schemes, implicit and explicit differencing schemes, and is capable of plane-parallel or cylindrical geometry simulations. In addition, the code has been modified and new subroutines were added to enhance its capabilities and extend them to model the complex ablation physical processes occurring in ablation fed PPTs [2]. In addition, new circuit solvers were added to help simulate advanced PPT circuitry [3].

MACH2 has been implemented to simulate the experimental data for the coaxial inverse-pinch PPT and to provide guidance for improving the performance of PPTs. Figure 21 show the MACH2 computational domain. The computational domain consisted of 7 blocks, this large number of blocks was necessary to accurately simulate the thruster's inter-electrode and plume regions.

Figure 4 presents a comparison between the experimentally measured and the MACH2 theoretically simulated PPT discharge current waveforms for 20 and 30 joule thruster energy operation. The comparison indicates good agreement between the two results for the first 10 μsec of the current pulse.

For 20 joule thruster operation, Figure 22 shows MACH2 current contours with the experimental values superimposed on the r-z plane current contour plots. Comparisons between the measured enclosed current magnitudes and the MACH2 predicted values for radial locations of 1.59, 2, and 3 cm for the different axial positions are made. For axial locations of 0, 0.5, and 1.0 cm, MACH2 predictions agree well with the experimental data, however, for axial locations of 1.5, 2, and 2.5 cm the MACH2 predictions deviate from the experimental data.

For 30 joule thruster operation, Figures 23 shows MACH2 current contours with the experimental values superimposed on the r-z plane current contour plots. Comparisons between the measured enclosed current magnitudes and the MACH2 predicted values for radial locations of 1.59, 2, and 3 cm for the different axial positions are made Again, as in the 20 joule thruster operation, for axial locations of 0, 0.5, and 1.0 cm, MACH2 predictions agree well with the experimental data, however, for axial locations of 1.5, 2, and 2.5 cm the MACH2 predictions do not agree with the experimental data. The discrepancy in the 20 and 30 joules thruster operation at axial locations greater than 1.5 cm can be attributed to loss of probe accuracy due to reduced magnetic field strengths. This loss of accuracy is mainly due to the fact that as the magnetic field strength diminishes, the EMI magnitude relative to the actual probe signal becomes significant thus resulting in greater error in the probe signal.

Figures 17, 18, 19, and 20 show a comparison between the experimental and MACH2 predicted temporal T_e and n_e profiles at a radial location of 2 and 3 cm at 6 cm from the thruster's exit plane at 20 joule thruster operation, respectively. From Figures 17 and 19, it is observed that for the first 7 μsec the experimentally measured ($(T_e)_{exp}$) is higher than MACH2 predicted value ($(T_e)_{MACH2}$), whereas, for the last 8 μsec $(T_e)_{exp}$ profiles matches the $(T_e)_{MACH2}$ profile within the accuracy of the measured signal. For n_e profiles, presented in Figures 18 and 20, the experimentally measured

($(n_e)_{exp}$) values do not agree with the MACH2 predicted ($(n_e)_{MACH2}$) values for the first 5 μsec of the signal, whereas, for the next 5 μsec there is good agreement between $(n_e)_{exp}$ and $(n_e)_{MACH2}$ values. For the final 5 μsec, the $(n_e)_{exp}$ and $(n_e)_{MACH2}$ values diverge mainly due to loss of accuracy on the current probe signals since the signal magnitude diminishes and that results in a loss of measurement accuracy since the probe settings are set for low sensitivity to capture all the probes' signal over the entire current magnitude range.

Figures 24 and 25 show the MACH2 predicted T_e and n_e profiles for radial locations of 1, 2, and 3 cm for axial locations of 2, 4, and 6 cm from the thruster's exit plane at 20 joule thruster operation. Results show that T_e values range between 3 and 6 eV, whereas, n_e values range between 10^{20} and 10^{21} m^{-3}.

CONCLUSIONS

A coaxial inverse-pinch pulsed plasma thruster (PPT) has been designed, fabricated, and tested. Experiments were performed to measure the thruster's discharge current, Teflon mass loss, radial and axial variations in the azimuthal magnetic field strength in the thruster's inter-electrode region, and T_e and n_e temporal profiles in the thruster's plume using Triple Langmuir probes. An azimuthally symmetric current distribution was attained for the following thruster configuration: Teflon radius of 1 cm, electrode radius of 1.35 cm with a 1.6 cm gap at a background pressure of $3X10^{-3}$ Torr. Teflon mass loss of 3.72 μg/pulse and 10.2 μg/pulse was measured for 20 and 30 joule thruster operation, respectively. T_e values between 3 and 8 eV and electron number n_e values up to 10^{21} m^{-3} were measured. The MACH2 2½ magnetohydrodynamic code was utilized to model the thruster operation. Experimental and MACH2 predicted results agreed well.

For future work the impulse-bit of a coaxial inverse-pinch PPT has to be measured in order to determine the thruster efficiency. To accomplish this, it is essential to achieve symmetric current distribution operation at background pressures lower than $5X10^{-6}$ Torr

ACKNOWLEDGMENTS

The authors gratefully acknowledge the assistance of Eric Pencil in facilitating the use of VF-3 at NASA Glenn Research Center. In addition, the assistance of James Coy from the Facilities and Engineering Division is acknowledged. This work was supported by NASA Glenn Research Center under NAG3-843. The support of the Ohio Supercomputer in providing essential computational resources is gratefully acknowledged.

REFERENCES

1. Benson, S.W., Arrington, L. A., Hoskins, W. A., and Meckel, N.J., "Developement of a PPT for the EO-1 Spacecraft," AIAA 99-2276, June 1999.

2. Mikellides, I.G., "Theoretical Modeling and Optimization of Ablation-Fed Pulsed Plasma Thruster," Ph.D dissertation, Columbus, Ohio Sept. 1999.

3. Kamhawi, H., Turchi, P.J., Mikellides, P.G., and Mikellides, I.G., "Experimental and Theoretical Investigation of an Inverse-Pinch Coaxial Pulsed Plasma Thruster," AIAA 00-3261, July 2000.

4. Haag, T. W., "PPT Thrust Stand", AIAA 95-2917, also NASA TM-107066, July 1995.

5. Kamhawi, H., and Turchi, P.J., "Design, Investigation, and Operation of an Inductively-Driven Coaxial Pulsed Plasma Thruster," IEPC 99-210, Oct. 1999.

6. Chen, S., and Sekiguchi, T., "Instantaneous Direct-Display System of Plasma Parameters by Means of Triple Probe," Journal of Applied Physics, Vol. 36 Mo. 8, Aug. 1965.

7. Tilley, D. L., Kelly, A. J., and Jahn, R. G., "The Application of the Triple Probe Method to MPD Thruster Plumes," AIAA 90-2667, July 1990.

8. Chung, P. M., Talbot, L., and Touryan, K. J., "Electric Probes in Stationary and Flowing Plasmas: Part 1. Collisionless and Transitional Probes," AIAA Journal, Vol. 12 No. 2, Feb. 1974.

9. Peterkin, R.E., Jr., and Frese, M.H., "MACH2: A Reference Manual - First Edition," Air Force Research Laboratory: Phillips Research Site, July 10, 1998.

Figure 1: Picture of coaxial inverse-pinch PPT with the ignition circuit

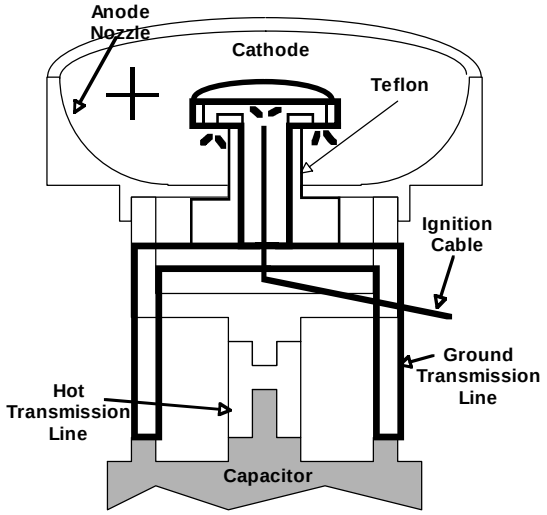

Figure 2: Schematic of coaxial inverse-pinch PPT

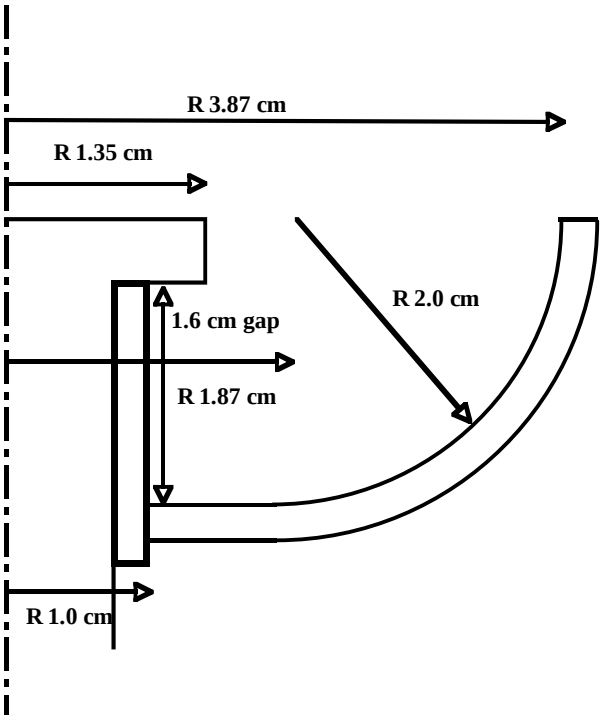

Figure 3: Schematic showing dimensions of coaxial inverse-pinch PPT inter-electrode region

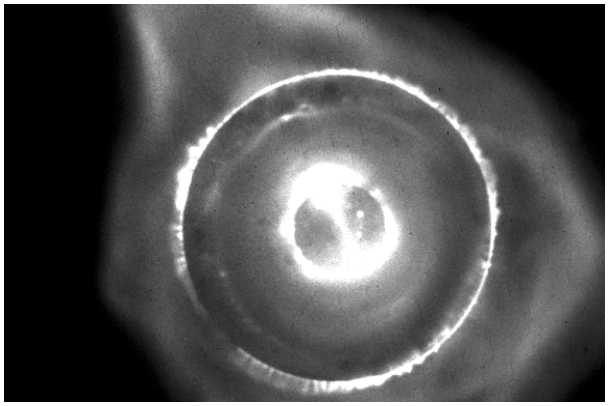

Figure 4: Discharge image 2.5 μsec after discharge initiation

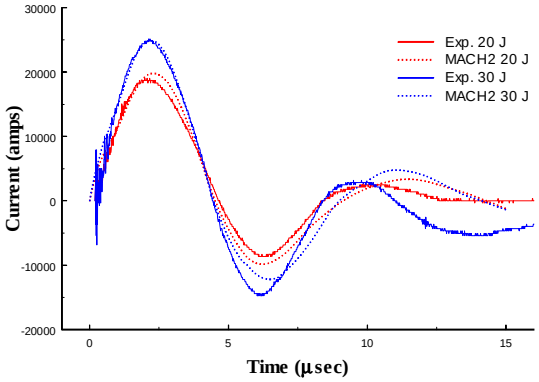

Figure 5: Experimental and MACH2 predicted PPT current waveforms for 20 and 30 joule operation

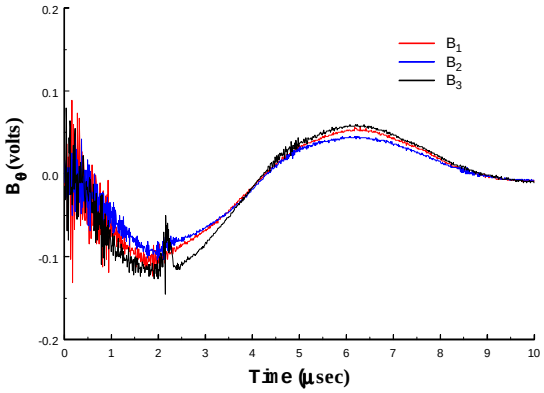

Figure 6: Azimuthal magnetic probe data at a radial location of 1.6 cm and an axial location of 0.15 cm from the nozzle electrode surface for 20 joule operation

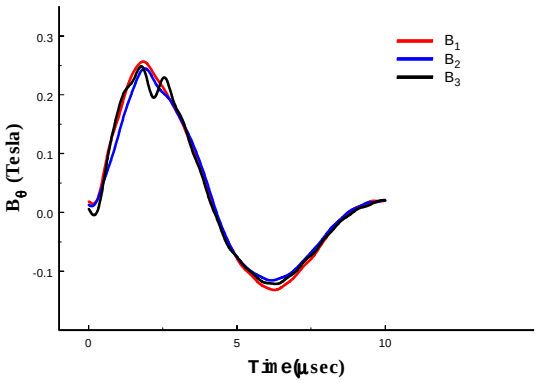

Figure 7: Azimuthal magnetic probe filtered data at a radial location of 1.6 cm and an axial location of 0.15 cm from the nozzle electrode surface for 20 joule operation

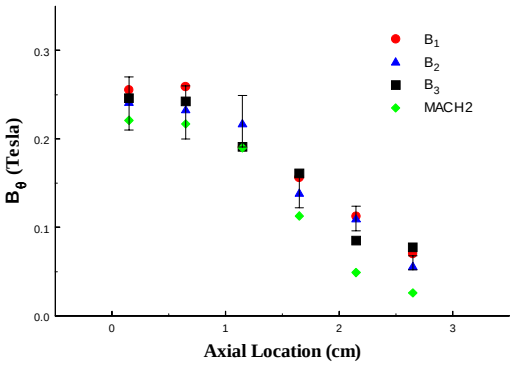

Figure 8: Azimuthal magnetic field mappings at a radial location of 1.59 cm for 20 joule operation

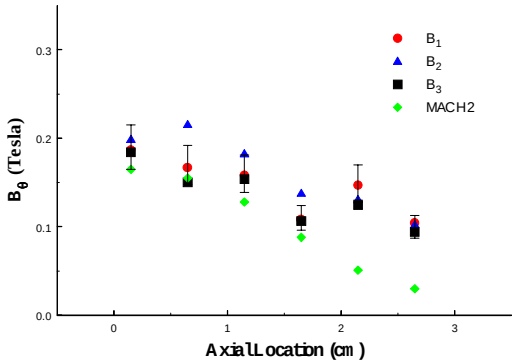

Figure 9: Azimuthal magnetic field mappings at a radial location of 2 cm for 20 joule operation

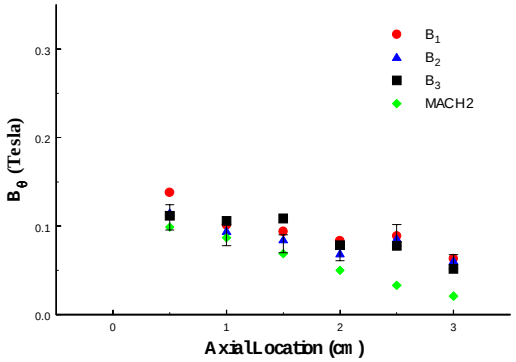

Figure 10: Azimuthal magnetic field mappings at a radial location of 3 cm for 20 joule operation

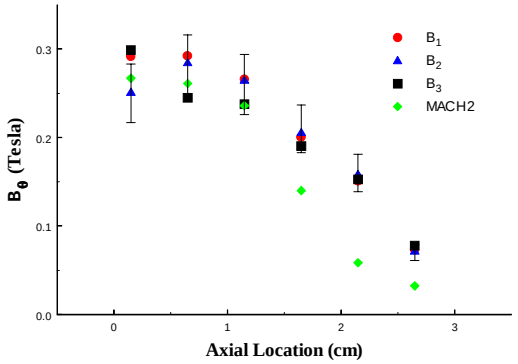

Figure 11: Azimuthal magnetic field mappings at a radial location of 1.59 cm for 30 joule operation

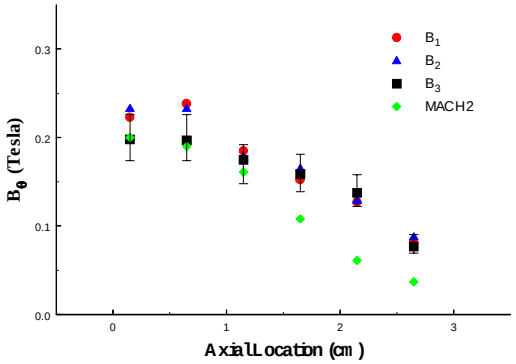

Figure 12: Azimuthal magnetic field mappings at a radial location of 2 cm for 30 joule operation

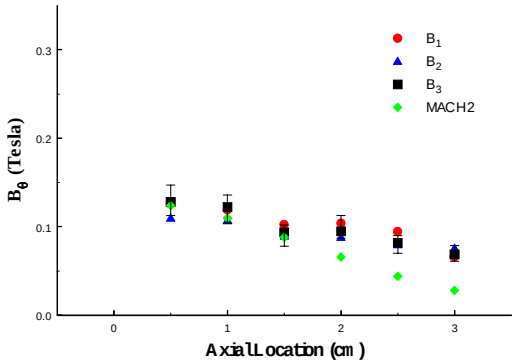

Figure 13: Azimuthal magnetic field mappings at a radial location of 3 cm for 30 joule operation

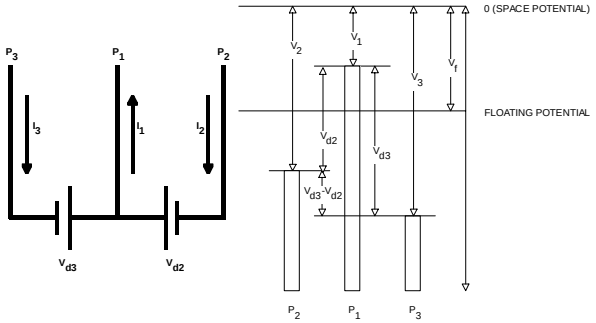

Figure 14: Circuit and potential diagrams for the triple-Langmuir probe.

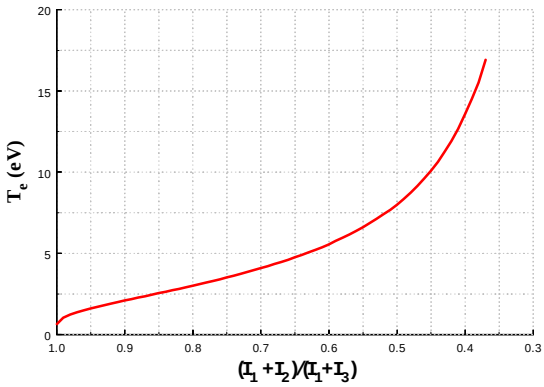

Figure 15: Curve for electron temperature T_e for different triple-Langmuir probe current ratios for V_{d2}=4.81 volt and V_{d3}=18.74 volt

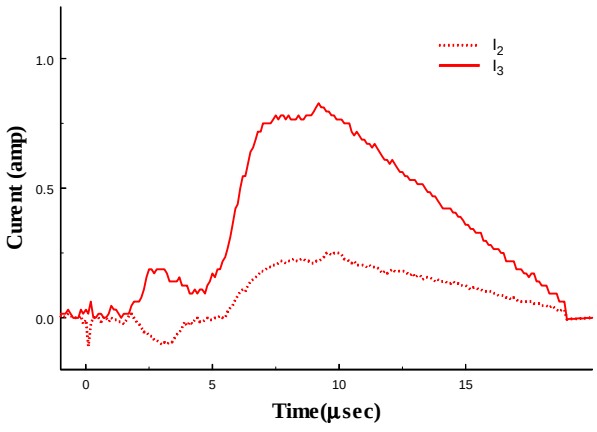

Figure 16: Triple-Langmuir probe Current waveforms at a radial location of 3 cm at 6 cm from thruster exit plane for 20 joule operation

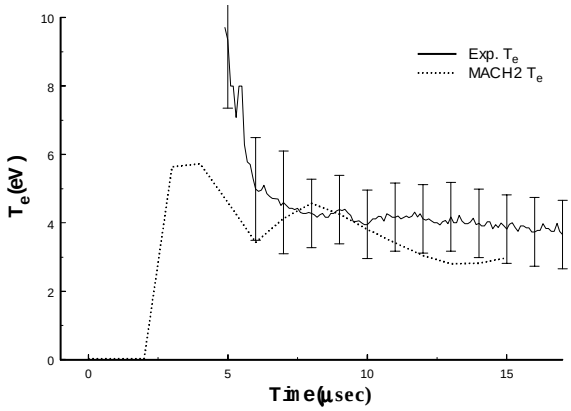

Figure 17:Experimental and MACH2 temporal T_e profiles at a radial location of 3 cm and an axial location of 6 cm from the thruster's exit plane for 20 joule thruster operation

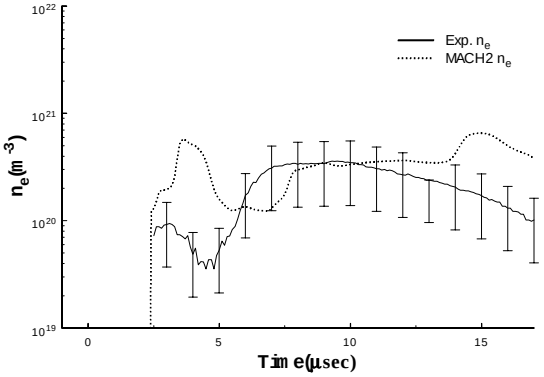

Figure 18: Experimental and MACH2 temporal n_e profiles at a radial location of 3 cm and an axial location of 6 cm from the thruster's exit plane for 20 joule thruster operation

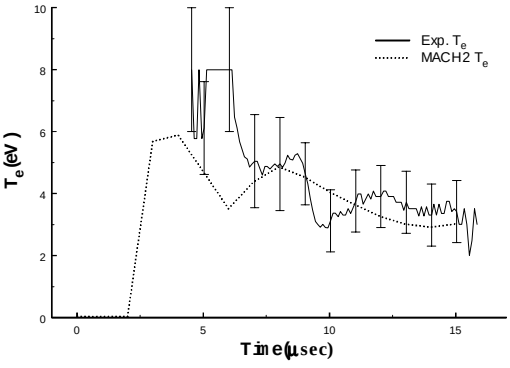

Figure 19:Experimental and MACH2 temporal T_e profiles at a radial location of 2 cm and an axial location of 6 cm from the thruster's exit plane for 20 joule thruster operation

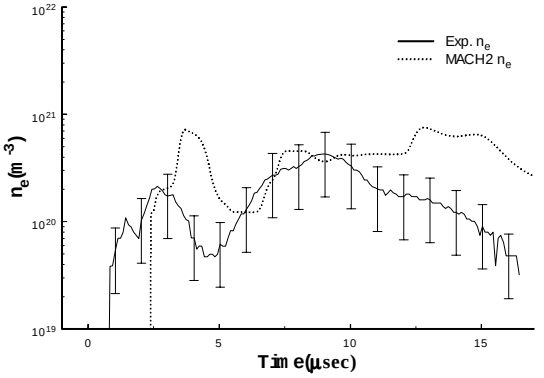

Figure 20: Experimental and MACH2 temporal n_e profiles at a radial location of 2 cm and an axial location of 6 cm from the thruster's exit plane for 20 joule thruster operation

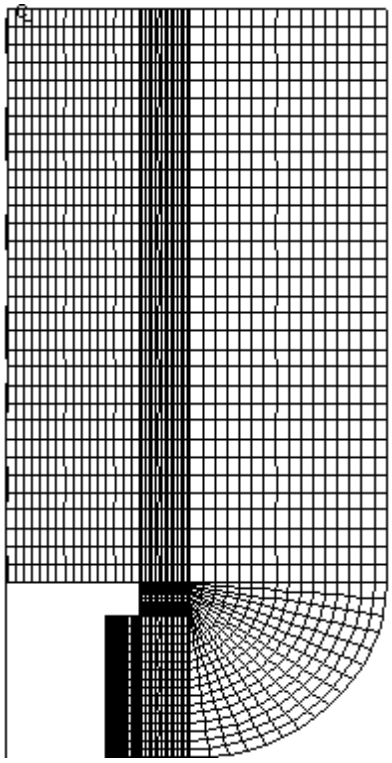

Figure 21: MACH2 computational domain.

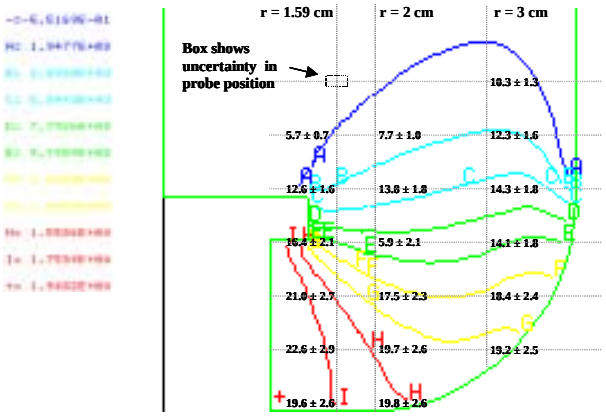

Figure 22:MACH2 current contours for 20 joule thruster operation with experimental data superimposed on the plot at the different measurement locations

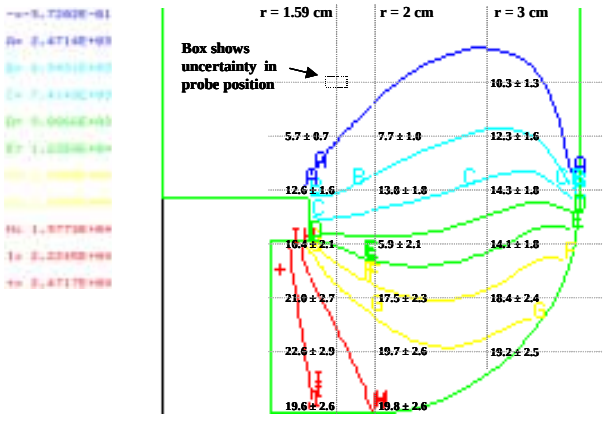

Figure 23: MACH2 current contours for 30 joule thruster operation with experimental data superimposed on the plot at the different measurement locations

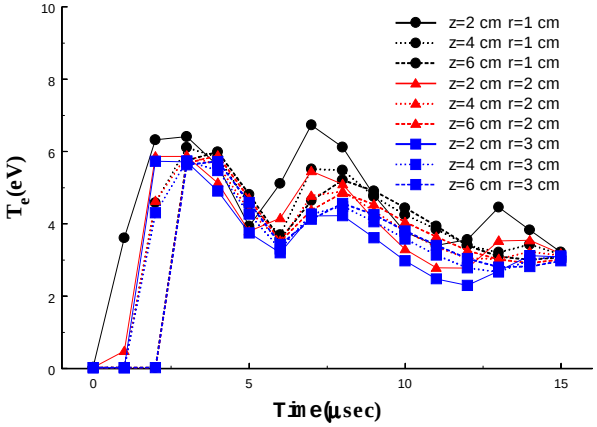

Figure 24: MACH2 predicted temporal T_e profiles for the different radial and axial locations for 20 joule operation

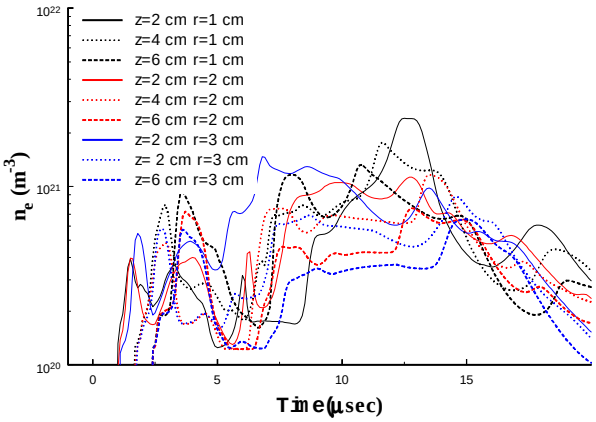

Figure 25: MACH2 predicted temporal n_e profiles for the different radial and axial locations for 20 joule operation